PROCEEDINGS OF SCIENCE

Operational Experience with the ATLAS Pixel Detector at the LHC

Markus Keil*
On behalf of the ATLAS Collaboration
II. Physikalisches Institut der Georg-August-Universität,
Friedrich-Hund-Platz 1, D-37077 Göttingen
and CERN, CH-1211 Geneva 23
E-mail: markus.keil@cern.ch

The ATLAS Pixel Detector is the innermost detector of the ATLAS experiment at the Large Hadron Collider at CERN, providing high-resolution measurements of charged particle tracks in the high radiation environment close to the collision region. This capability is vital for the identification and measurement of proper decay times of long-lived particles such as b-hadrons, and thus crucial for the ATLAS physics program. The detector provides hermetic coverage with three cylindrical layers and three layers of forward and backward pixel detectors. It consists of approximately 80 million pixels that are individually read out via front-end chips bump-bonded to 1744 n-on-n silicon pixel sensors. In this paper results from the successful operation of the Pixel Detector at the LHC will be presented, including calibration procedures, detector performance and measurements of radiation damage. The detector performance is excellent: more than 95% of the pixels are operational, noise occupancy and hit efficiency exceed the design specification, and a good alignment allows high quality track resolution. Clear indications of radiation damage are observed, which are in good agreement with model predictions.

The 21st International Workshop on Vertex Detectors
16-21 September 2012
Jeju, Korea

*Speaker.

© Copyright owned by the author(s) under the terms of the Creative Commons Attribution-NonCommercial-ShareAlike Licence.

PoS(Vertex 2012)049

1. The ATLAS Pixel Detector

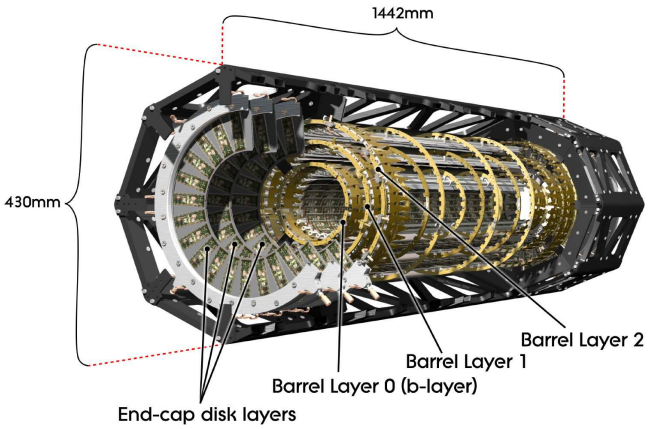

Figure 1: Schematic drawing of the ATLAS Pixel Detector. The detector comprises three concentric barrel layers and two end-caps with three discs each. The single detector modules are mounted on carbon fibre support structures with incorporated cooling circuits [1].

The ATLAS Pixel Detector, shown in Fig. 1, is the innermost tracking detector of the ATLAS experiment [2]. It is made of three concentric barrel layers with mean radii of 50.5 mm, 88.5 mm and 122.5 mm centred around the beam axis and two endcaps with three discs each, forming a three-hit system up to pseudo-rapidities of ± 2.5. The full detector contains 1744 pixel modules, which are mounted on carbon fibre supports. An evaporative C_3F_8 cooling system is incorporated into the local supports to absorb the heat produced by the modules and to allow for an operation at temperatures below 0°C, to limit the effects of radiation damage.

The pixel modules (Fig. 2) are made of a 250 μm thick n-on-n silicon sensor, 16 front-end chips and a module controller chip (MCC). The sensor is divided into 47,232 pixels with a typical pixel size of 50 μm $\times$ 400 μm; approximately 10% of pixels have a size of 50 μm $\times$ 600 μm to bridge the gaps between the readout chips. The sensor is read out by 16 front-end chips with 2880 electronics channels each. Each pixel cell contains a charge sensitive preamplifier, a discriminator and the necessary readout logic to transfer hits to the peripheral logic of the chip, the end-of-column (EOC) logic. In the EOC logic hits are stored up to the programmable trigger latency and sent to the module controller chip in case a trigger arrives at the correct latency, erased otherwise. Together with the mere hit location and time, the time-over-threshold (ToT) information is read out for each hit. This is the time interval during which the preamplifier output is above the threshold, in units of the bunch crossing clock (a bunch crossing (BC) in this context always denotes a 25 ns clock cycle, even if collisions happen at a lower frequency). Due to the pulse shape of the preamplifier the ToT is a nearly linear function of the deposited charge. Evaluating this ToT information can therefore be used to infer the charge deposited by a passing particle.

The routing of signals and power lines of the module is done on the flex hybrid. This is a flexible kapton PCB, which is glued onto the backplane of the sensor. The connection to the

PoS(Vertex 2012)049

front-end chip is made with wire bonds. The flex hybrid also carries the MCC, which controls the front-end chips and performs an event building with the hit data received from the front-end chips. The off-module connection is provided by a micro cable (type-0 cable), which is either soldered directly onto the flex hybrid (in case of the disc modules) or connected to a kapton pigtail (in case of the barrel module). Figure 2 shows the elements of a pixel barrel module.

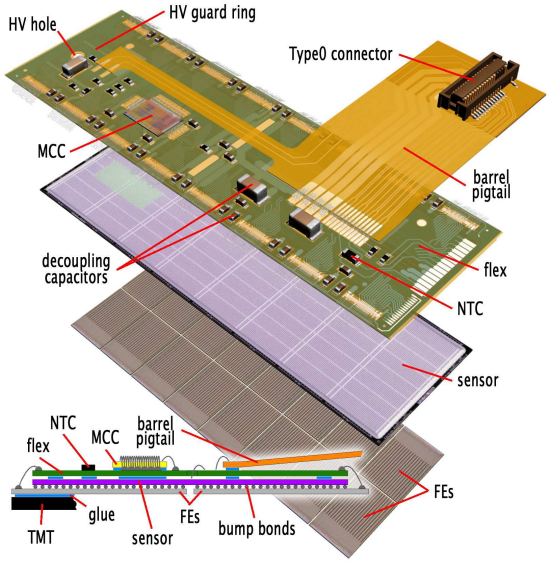

Figure 2: Assembly view and cross section of an ATLAS Pixel Detector module. Sixteen front-end chips are bump bonded to the silicon pixel sensor. Interconnections are done on a flexible kapton PCB, which is connected by wire bonds to the electronics chips [2].

The transmission of fast signals (data, clock and commands) between the detector and the readout crates in the counting rooms is achieved via optical links. One TTC link per module (Timing, Trigger and Commands) carries the clock and commands to the detector, a data link brings the hit data from the detector to the readout crates. Most modules have one associated data link, only the modules in the innermost barrel layer have two data links per module to accommodate the higher data rate. The electro-optical conversion on the detector side is done on optoboards, which are located at a distance of approximately 1 m from the interaction point.

2. Operational Aspects

The complete ATLAS Pixel Detector has been operated for the first time in the experiment in August 2008, shortly before the arrival of the first beam in the LHC. Since then the detector operation has continued without any major problems. Currently 95.4% of the detector is active. The non-active part contains 77 disabled modules (4.4%) and 47 disabled front-end chips (0.17%). It has been found that in particular the front-end failures are linked to thermal cycles of the detector.

With the accelerator performing extremely well, reaching luminosities of approximately $7 \times 10^{33}\,\mathrm{cm}^{-2}\mathrm{s}^{-1}$, however with a bunch spacing of 50 ns instead of 25 ns, the detectors are now facing pile-up that exceeds the design value. This poses a notable challenge to the readout of the pixel

PoS(Vertex 2012)049

detector and we are exploiting all possibilities of the readout system to detect and correct possible problems in real-time.

To protect the front-end electronics from the effects of beam incidents a "stable beam" interlock has been implemented. Until stable beams are declared by the LHC the sensor high voltage is switched off. This avoids that a high local charge deposition in the pixel sensors creates a short circuit between the sensor bias voltage and the input of the preamplifiers. Since the switching off of the high voltage would normally lead to noise in the electronics chips, the preamplifiers are also switched off. Once stable beams are declared, after additional checks of the beam conditions, the high voltage is ramped up and the preamplifiers are switched on. This warm-start procedure is performed with a paused trigger after the ATLAS data acquisition has been started, since the time necessary for the warm-start is of the order of one minute whereas the time needed to restart the ATLAS DAQ would be significantly longer.

3. Calibration Performance

The electronics parameters of the front-end pixel cells are assessed by means of a programmable charge injection circuit in the front-end chip. The timing and the amount of charge can be freely chosen, allowing to perform all necessary tunings and a wide range of measurements.

3.1 Threshold and Noise

Threshold and noise of the analogue part are measured by injecting amounts of charges around the expected threshold. For each charge the number of hits for a fixed number of injections are counted. The values of threshold and noise are then extracted from an error function fit to the obtained response curve.

In order to set the thresholds as homogeneously as possible, a similar scan is performed. However for this so-called threshold tuning the injected charge is fixed to the target threshold value and in each pixel the setting of the tune-DAC, which determines the discriminator threshold, is varied. The setting, for which the pixel's response fraction, i.e. the ratio of hits per injection, is as close as possible to 50%, is the ideal setting for the given target threshold.

Figure 3 (a) shows the measured threshold values of all scanned pixels in the detector, after a tuning with a target threshold of 3500 e. We see that most pixels are well-centred around the target threshold value, the typical RMS of the threshold distribution after tuning is $\sim$ 40 e.

The noise values obtained from the same threshold scan are shown in Fig. 3 (b). The behaviour is clearly different between the normal pixels and long or ganged sensor pixels at the edges of the front-end chips. This expected effect is due to the higher load capacitance those sensor pixels pose to the electronics. Typical noise values vary between $\sim$ 180 e for normal pixels and $\sim$ 300 e for ganged pixels. In terms of the ratio between threshold and noise this leads to values of $\sim$ 20 for the normal pixels and $\sim$ 12 for the ganged pixels. The high noise values in the tails of the distribution, visible in the logarithmic plot, have been traced back to regions with merged bumps (see below) at the edges of some sensors.

Pixels exceeding a noise occupancy of 10^{-5} hits/event in dedicated noise data taking runs are masked for ATLAS data taking already in the module configuration. Typically 0.1% of all pixels are masked at a threshold setting of 3500 e. On a run-by-run basis remaining noisy pixels

PoS(Vertex 2012)049

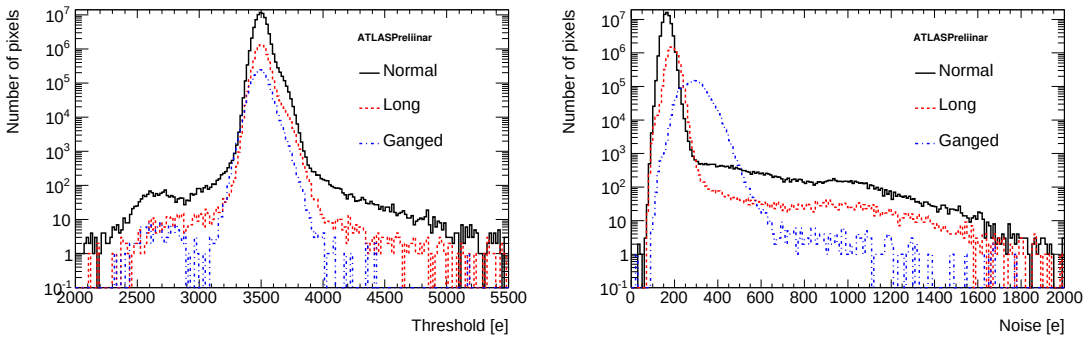

(a) (b)

Figure 3: (a) Measured threshold values for all scanned pixels in the detector. Prior to the scan the threshold settings have been tuned to 3500 e. (b) Noise values obtained from the same threshold scan [3].

(typically 0.01% – 0.02% of all pixels) are determined in the first-pass reconstruction and then masked offline for the bulk reconstruction. After masking, the noise occupancy is of the order of 10^{-10} hits/pixel/event, whereas the noise in the raw data is approximately of 10^{-8} hits/pixel/event or O(1 hit per event) in the full detector, respectively.

3.2 Charge Measurement

As described above, the ToT information stored together with each hit can be used as a measure for the deposited charge. In order to use the ToT for the charge measurement it has to be calibrated. This is done in a similar manner to the threshold scan, but with an enlarged charge range, using charges above threshold up to twice the charge of a minimum ionising particle (mip). The curve of average ToT vs. injected charge is fit with a simple, invertible function, which is then used in the offline reconstruction to calculate the charge from the measured ToT values. To save storage space, only one calibration function is saved per front-end chip and pixel-type. It is therefore desirable that the ToT response is as homogeneous as possible between the pixels of a front-end chip. This is achieved by tuning the feedback current with a global 8-bit DAC on each front-end chip and an additional 3-bit DAC in each pixel cell.

Figure 4 (a) shows the measured ToT values for all pixels in the detector for an injected charge corresponding to one mip. The figure compares the values measured after tuning in the experiment and those obtained with a configuration determined from a production tuning (The RMS for completely untuned modules is significantly larger, typically between 2 and 3 bunch crossings). The plot shows that after tuning the ToT is close to the target value of 30 bunch crossings, with an RMS of less than 1 bunch crossing. As an application of the pixel ToT Fig. 4 (b) shows the dE/dx for tracks with at least three pixel hits. The dE/dx has been determined from the cluster charges in a truncated mean method. The bands for pions, kaons and protons are clearly visible.

3.3 Timing

For an efficient reconstruction the hits of particle tracks not only need to be detected but also assigned to the correct interaction. This requires a time resolution of better than 25 ns. On the front-

PoS(Vertex 2012)049

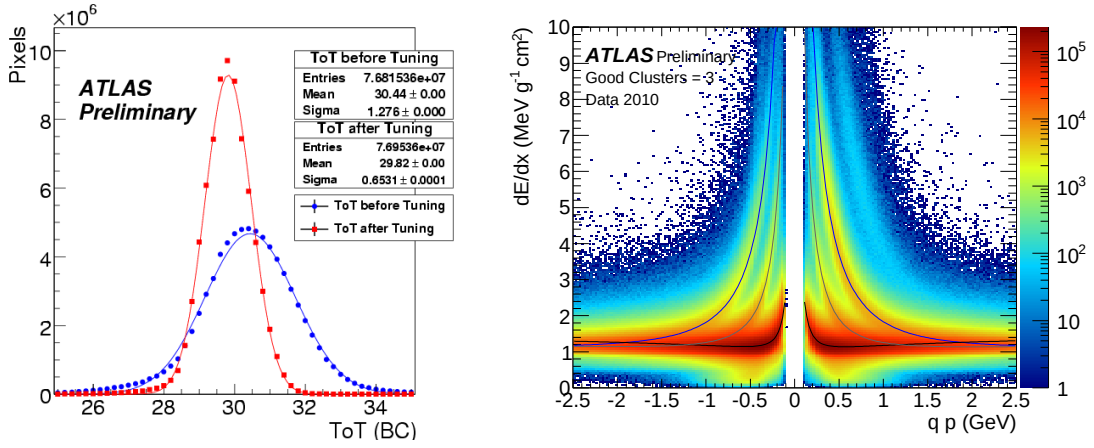

(a) (b)

Figure 4: (a) Average ToT for a 20 ke charge injection in all pixels of the detector. Circles show the distribution using an "old" configuration from production scans, squares the distribution after re-tuning in the experiment [3]. (b) Track dE/dx determined from the pixel ToT in a truncated mean method. The plot contains tracks with three or more good pixel clusters. The superimposed curves are the most probable values calculated using the masses of pions (black), kaons (gray) and protons (blue) [7].

end level the timing accuracy is limited by the timewalk, i.e. the effect that the preamplifier pulses for small deposited charges cross the discriminator threshold later than those for large charges. This leads to an uncertainty in the detection time for different signals belonging to the same collision. The critical quantity to quantify this effect is the so-called in-time threshold, i.e. the smallest charge that is detected within the same bunch crossing as a large reference charge. A measurement of the in-time threshold values for all pixels in the detector is shown in Fig. 5. Without corrections the average in-time threshold is 4800 e, approximately 1300 e above the discriminator threshold of 3500 e. Charges between 3500 e and 4800 e are detected but not assigned to the correct bunch crossing. This behaviour can be improved by a hit-doubling mechanism implemented in the FE-I3 chip. This mechanism uses the ToT information of each hit to determine whether it is likely to have suffered a timewalk of at least 1 BC. In case the ToT is below a programmable threshold the hit is written twice into the buffers, once with unchanged timing information and once one BC earlier. This mechanism allows to reduce the in-time threshold to a value 200 – 300 e above the discriminator threshold, as shown by the second histogram in Fig. 5, at the cost of a slight ($\sim$ 10%) increase in the occupancy.

On the system level both the homogeneity between the modules and the stability of the timing have been examined. To improve the homogeneity a sub-ns delay can be added to the clock and data lines of each individual module. This has been done, taking into account the different cable delays and the different time of-flight for the different parts of the detector. After a final adjustment using collision data, a measurement of the detection time for large charges yields an RMS of 0.007 BC or 175 ps. This remaining module-to-module variation is of the order of the step width of the delay used for adjustment and therefore expected. The stability of the module timing can be assessed from the stability of scans of the optical links used for data transmission. Evaluation of several of

PoS(Vertex 2012)049

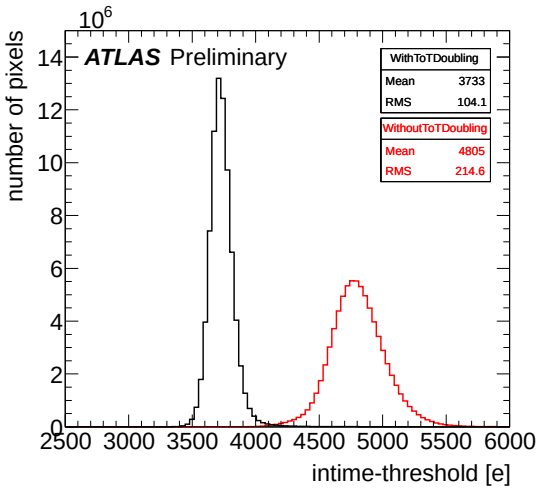

Figure 5: Measured in-time threshold for the full Pixel Detector with (black curve) and without (red curve) hit-doubling. The discriminator threshold was set at 3500 e [3].

these scans over a period of 3 weeks has shown that for nearly all modules the maximal timing variation is below 2 ns. Both the module-to-module variations and the variations over time are tolerable as a 5 ns safety margin has been considered in the timing settings: the delay settings are such that the detection time of a large charge, i.e. a charge not suffering timewalk, is 5 ns after the beginning of the clock cycle. This leaves 20 ns margin for timewalk and 5 ns for random variations of the detection time, well above the experimentally observed variations.

3.4 Bump Quality

For particle detection with a hybrid pixel detector it is important that each sensor pixel is connected with its corresponding electronics channel by a bump bond. The bump quality is assessed by a combination of different calibration measurements. Disconnected bumps are identified by the missing cross-talk between neighbouring pixels and the lower noise of the electronics pixel: the first condition uses the fact that the cross-talk of an injected charge between two neighbouring pixels happens through the sensor pixel and thus two intact bump bond connections are necessary to observe cross-talk hits; the second condition uses the decreased load capacitance at the preamplifier if a sensor pixel is not connected. The method is nicely illustrated by Fig. 6, which shows the results for both calibration measurement for the same module. For illustration a particularly bad module was chosen and one clearly sees a region of disconnected pixels in both calibraton scans.

Pixels which are responding to digital injections but not to injections of analogue test charges are considered candidates for merged bumps. The fractions of pixels affected by both types of bump-bonding problems are of the order of 0.1%. No deterioration with operation has yet been observed.

4. Monitoring of Radiation Damage

It is expected that the detector behaviour changes with time due to radiation damage effects.

PoS(Vertex 2012)049

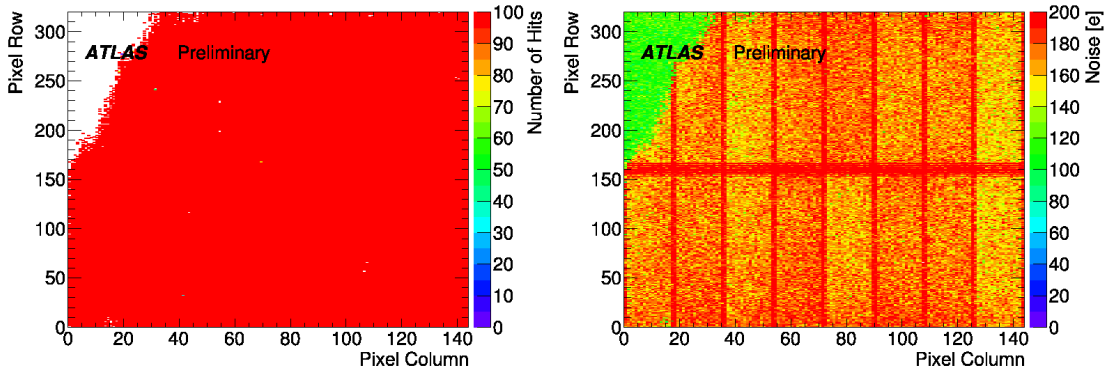

(a) (b)

Figure 6: (a) Measured number of crosstalk hits and (b) noise values for a particularly bad module. The pixels in the upper left corner of the module show no crosstalk hits and low noise values and are therefore candidates for disconnected bumps. The bump problems shown in this module are known from production [3].

At the current (December 2012) integrated luminosity of $27\,\mathrm{fb}^{-1}$ both the reverse-bias current of the sensors and the voltage needed for full depletion show clear signs of radiation-induced changes. To follow the evolution of the radiation damage and compare it with the models several methods have been implemented:

- Leakage current: The reverse-bias current of the sensors is measured at three different levels: one measurement is provided by the power supplies. In addition, a fraction of the high voltage lines is equipped with current measurement devices, which provide a measurement of the sensor leakage current per module with a precision of approximately 20 nA. Finally, the front end chips provide the possibility to measure the single pixel leakage current by means of a calibration scan. The range of this measurement has been optimised by design for the leakage current of irradiated sensors with a least significant bit of 0.125 nA. All measurements show a clear increase of the radiation-induced current, in good agreement with the expectations. Figure 7 (a) shows the evolution of the average bias current for the three barrel layers, as measured with the high voltage power supplies, together with the model predictions. One sees a nice qualitative agreement, including the decrease of the current due to annealing during warm-up periods. The predictions of the model were scaled up by 15% for Layer 0 and by 25% for Layers 1 and 2 to obtain quantitative agreement. These changes are within the expected uncertainties of the model and the measurement.

- Depletion voltage: before type inversion, when the depletion region grows from the backside of the sensor, the depletion voltage is measured by means of a calibration measurement. The procedure measures the cross-talk for different bias voltages and uses the fact that the coupling of neighbouring pixels changes when the depletion region reaches the segmented side. After type inversion the depletion voltage can be measured from inclined tracks in a bias voltage scan [4]. Both measurement methods indicate that the pixel sensors in the innermost

PoS(Vertex 2012)049

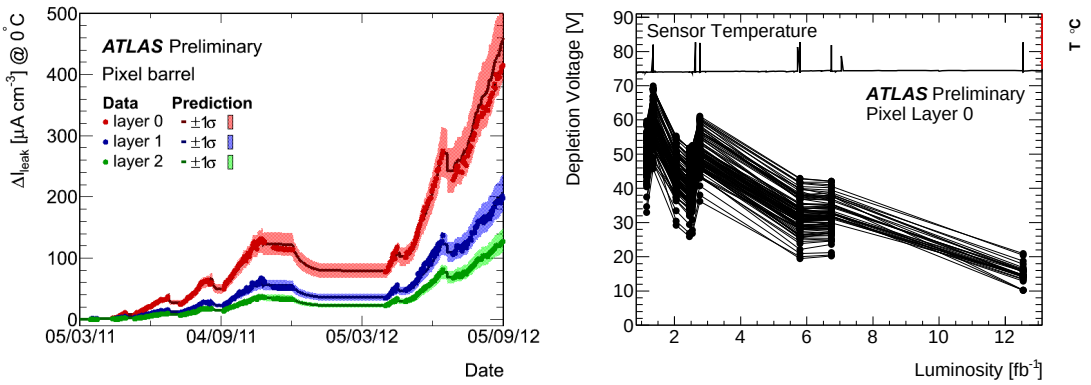

(a) (b)

Figure 7: (a) Average reverse-bias current in the three barrel layers of the ATLAS Pixel Detector vs. time. The model predictions have been scaled up by 15% (Layer 0) or 25% (Layer 1 and 2), respectively. (b) Depletion voltage of the modules in Layer 0, measured with the cross-talk method, vs. integrated luminosity. The inset on the top shows the average temperature during the period with clear indication of the high temperature period corresponding to short and long cooling stops [3].

barrel layer have undergone type inversion, again in good agreement with the expectation. The evolution of the depletion voltage, as measured with the cross-talk method is shown in Fig. 7 (b) for all modules of the innermost barrel layer. One sees the expected decrease of the depletion voltage with increasing integrated luminosity as well as the beneficial annealing during periods without cooling. The lower number of points at 12.5 fb^{-1} is due to the fact that the modules were close to type inversion so that the depletion voltage could not be measured any longer with this method.

The model predictions that were used are based on FLUKA simulations as well as on the measured luminosity and temperature profiles [5]. A more comprehensive overview of the observed radiation damage and comparisons between measurements and models can be found in [6].

5. Examples of the Offline Performance

One of the most important aspects of the detector performance is the efficiency. This is shown in Fig. 8. The figure shows the efficiency at which for a reconstructed track a hit can be found on the different detector layers. The efficiency is approximately 99% on most parts of the detector. The lower efficiency in the outermost discs is due to single bad modules, known from production. The 100% efficiency for Layer 0 ("B-layer") is an artefact of the track selection and therefore this measurement point cannot be taken into account. Disabled modules have been excluded from the efficiency calculation.

The spatial resolution can be compared with the expectation in the so-called (unbiased) residual distributions. To obtain the unbiased residuals tracks are reconstructed, excluding the information of the detector layer under study. The residual is given by the difference between the extrapolated track point and the measured track point in this layer. Figure 9 shows the residual

PoS(Vertex 2012)049

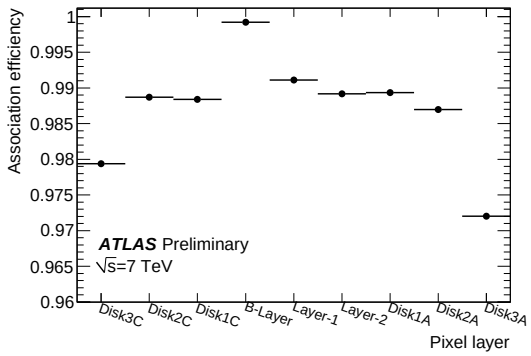

Figure 8: Hit association efficiency for the different parts of the ATLAS Pixel Detector. The high efficiency of the B-layer is an artefact of the track set used for the measurement, whereas the low efficiency of the outermost discs is due to few bad modules known from production [8].

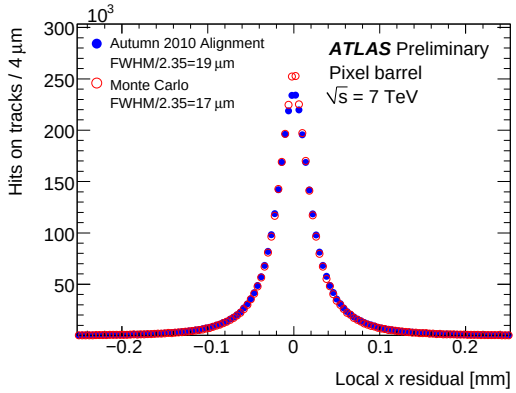

Figure 9: Residuals between extrapolated and measured track position in the Pixel Detector barrel, for the 50 μm pixel direction. Closed circles show data, open circles simulation results for a perfectly aligned detector [9].

distribution for the pixel barrel, for the 50 μm pixel direction. The distribution has been obtained using the latest alignment and is in good agreement with the simulated distribution for a perfectly aligned detector.

Due to the magnetic field in the tracker volume the charge carriers in the silicon sensors do not drift parallel to the electric field lines but at the so-called Lorentz angle. This angle, which is needed to determine the exact position of the primary particle, can be determined from the cluster sizes. Figure 10 shows the average cluster width vs. the track incidence angle of the primary particle. Due to the magnetic field effect, the minimal cluster size is not at perpendicular track incidence, but the minimum is shifted by the Lorentz angle. The value of the Lorentz angle determined from this method is (211.3 ± 1.6) mrad which is close to the expected value of approximately 225 mrad. The Pixel Detector has been operated at different temperatures since its installation. This has allowed the study of the temperature dependence of the Lorentz angle, which was found to match the expectations.

PoS(Vertex 2012)049

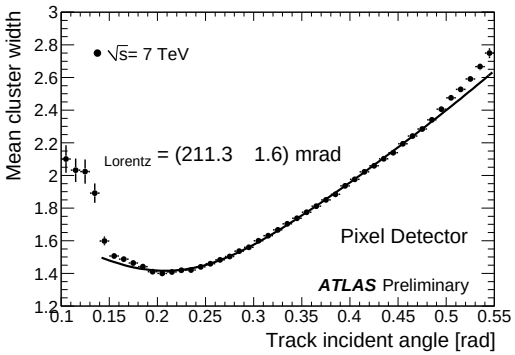

Figure 10: Average cluster width in the Pixel Detector barrel vs. the track incidence angle. Due to the magnetic field the minimum is not at perpendicular incidence, but shifted by the Lorentz angle [8].

6. Summary

Since its commissioning in 2008, the ATLAS Pixel Detector has been successfully operated in the ATLAS Experiment, currently with $\sim 4\%$ of the modules disabled. Most aspects of the detector behaviour are well understood and satisfy the requirements both concerning the electronics and module behaviour and the overall tracking performance. The low threshold dispersion of ~ 40 e and the electronic noise below 200 e lead to a noise occupancy of the order of 10^{-8} hits/pixel/BC. Using the timewalk correction of the ATLAS Pixel front-end chip, the in-time threshold is approximately 250 e above the discriminator threshold. The performance of the charge measurement by means of the time over threshold method has been demonstrated. The efficiency of the enabled modules measured in data taking with particle tracks is 99%, the spatial single-point resolution is according to the expectation.

Measurements of the reverse-bias current and the depletion voltage of the silicon sensors show clear signs of radiation-induced changes, which are in good agreement with the model predictions.

References

[1] G. Aad et al., *ATLAS Pixel Detector Electronics and Sensors*, *JINST* **3** P07007 (2008).

[2] ATLAS Collaboration, *The ATLAS Experiment at the CERN Large Hadron Collider*, *JINST* **3** S08003 (2008).

[3] Compilation of ATLAS Pixel results, https://twiki.cern.ch/twiki/bin/view/AtlasPublic/ApprovedPlotsPixel.

[4] A. Schorlemmer, *Monitoring radiation damage in the ATLAS Pixel Detector*, Proceedings of iWoRID 2012 - 14th International Workshop on Radiation Imaging Detectors, Submitted for publication to *JINST*.

[5] O. Krasel, *Charge Collection in irradiated Silicon Detectors*, PhD Thesis, Dortmund University (2004).

[6] S. Gibson, *Radiation Damage to Currently Running LHC Silicon Detectors*, These proceedings.

PoS(Vertex 2012)049

[7] ATLAS Collaboration, *dE/dx measurement in the ATLAS Pixel Detector and its use for particle identification*, ATLAS Technical Note ATLAS-CONF-2011-016 (2011).

[8] Compilation of ATLAS Pixel results, https://twiki.cern.ch/twiki/bin/view/AtlasPublic/PixelPublicResults.

[9] Compilation of ATLAS Inner Detector results, https://twiki.cern.ch/twiki/bin/view/AtlasPublic/InnerDetPublicResults.

PoS(Vertex 2012)049